

Image processing for cameras with fiber bundle image relay

Stephen J. Olivas,^{1,*} Ashkan Arianpour,¹ Igor Stamenov,¹ Rick Morrison,²
Ron A. Stack,² Adam R. Johnson,² Ilya P. Agurok,¹ and Joseph E. Ford¹

¹Photonic Systems Integration Laboratory, Electrical Engineering Department, University of California at San Diego, 9500 Gilman Dr., La Jolla, California 92093, USA

²Distant Focus Corporation, 4114B Fieldstone Road, Champaign, Illinois 61822, USA

*Corresponding author: stephenjolvivas@gmail.com

Received 24 October 2014; revised 21 December 2014; accepted 22 December 2014;
posted 5 January 2015 (Doc. ID 225588); published 6 February 2015

Some high-performance imaging systems generate a curved focal surface and so are incompatible with focal plane arrays fabricated by conventional silicon processing. One example is a monocentric lens, which forms a wide field-of-view high-resolution spherical image with a radius equal to the focal length. Optical fiber bundles have been used to couple between this focal surface and planar image sensors. However, such fiber-coupled imaging systems suffer from artifacts due to image sampling and incoherent light transfer by the fiber bundle as well as resampling by the focal plane, resulting in a fixed obscuration pattern. Here, we describe digital image processing techniques to improve image quality in a compact 126° field-of-view, 30 megapixel panoramic imager, where a 12 mm focal length $F/1.35$ lens made of concentric glass surfaces forms a spherical image surface, which is fiber-coupled to six discrete CMOS focal planes. We characterize the locally space-variant system impulse response at various stages: monocentric lens image formation onto the 2.5 μm pitch fiber bundle, image transfer by the fiber bundle, and sensing by a 1.75 μm pitch backside illuminated color focal plane. We demonstrate methods to mitigate moiré artifacts and local obscuration, correct for sphere to plane mapping distortion and vignetting, and stitch together the image data from discrete sensors into a single panorama. We compare processed images from the prototype to those taken with a 10 \times larger commercial camera with comparable field-of-view and light collection. © 2015 Optical Society of America

OCIS codes: (110.0110) Imaging systems; (100.0100) Image processing; (110.1758) Computational imaging.

<http://dx.doi.org/10.1364/AO.54.001124>

1. Introduction: Traditional Imagers and Fiber-Coupled Imagers

Traditional imaging systems form images onto flat image sensors, a difficult design constraint for wide-angle imaging in which off-axis aberrations dominate. A monocentric lens, where all optical surfaces are spherical and share a common center of curvature, images without coma or astigmatic aberration and significantly reduces imager volume (Fig. 1) [1,2].

This comes at a cost of forming a spherical image surface, which is incompatible with conventional image sensor fabrication technology [3]. Fiber optic bundles, a dense array of high index optical fibers with thin low index cladding, can be used to incoherently transfer optical power between an input and output surface [4,5].

This technique was used to couple the spherical image surface from a 60° field-of-view monocentric lens to one or more 221 kpixel CCD sensors with 23 μm pitch pixels [6]. More recently, the same basic structure has been applied to double the lens field-of-view and couple the image to high-resolution CMOS

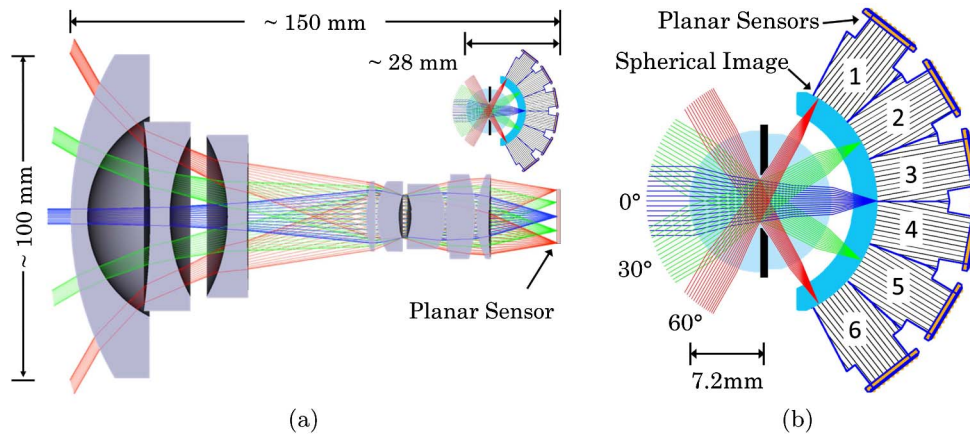


Fig. 1. (a) Conventional lens forms an aberrated planar image (the prototype is inset to show relative size). The Zebase design F_005 has been reoptimized to achieve $f = 12$ mm, $F/1.7$, and 120° field-of-view. (b) Prototype: a monocentric lens forms low-aberration spherical images but requires fiber bundles to relay the image to flat sensors.

sensors [7,8]. The lens, fiber bundle, and fiber-coupled sensor are shown in Fig. 2, and a more detailed view of the structure of the fiber bundle and sensor is shown in Fig. 3. Signal acquisition in such fiber-coupled imagers results from a cascade of optical processes. A continuous image is formed by the lens on the fiber bundle surface, where the local signal coupling may be strongly space variant according to the quasi-periodic fiber bundle structure. This signal is transferred through the multimode fiber core, where it loses all spatial coherence then is emitted from the output face of the fiber. In general, there can be a small free space gap (an air space or thickness of isotropic adhesive) between the rear face of the fiber and the focal plane, and the signal emission into this region can depend sensitively on launch conditions and wavelength. Finally, this signal is captured by the regular sampling grid of the focal plane sensor. If the fiber pitch is much smaller than the sensor pixels, this image acquisition “cascade” might be neglected. To achieve the highest possible spatial resolution, however, both fiber bundle and pixel pitch need to be minimized. Understanding each step of the image acquisition process can enable a broader class of computational image processing techniques.

Here, we present the first (to our knowledge) systematic characterization of the spatially variant impulse response at various stages within a fiber-coupled imager (an imaging system that uses fiber bundle image relay). We use a fiber-coupled monocentric lens camera prototype to investigate computational imaging techniques applicable to any imaging system that uses fiber bundles to relay or field-flatten images onto planar image sensors as well as system-specific issues related to combining multiple sensors to form visually seamless panoramas. Section 2 is devoted to an in-depth investigation of the local image transfer characteristics of each component within the prototype. Section 3 describes the methods we employed to globally remove image artifacts due to fiber optic bundle image transfer and system components. Section 4 shows the results of mapping the spherical image space to a planar space and how to form panoramas by aligning and stitching contiguous sensor data. Section 5 explains the experimental setup under which data is collected for camera calibration and performance measurements. Section 6 discusses our experimental results from the prototype imager and compares the performance to a much larger conventional digital SLR “benchmark” camera (Fig. 4).

2. Component and System Point Spread Function

We characterized our custom monocentric lens fabricated by Optimax (focal length $f = 12$ mm, $F/ = 1.35$) [Fig. 2(a)] [9] and compared it to a high-resolution Nikon LU Plan APO 150X microscope objective ($f = 1.33$ mm, numerical aperture $NA = 0.9$). Both of these objectives were used with the following devices under test (DUTs) to sample the image formed: a 24AS Schott fiber bundle [Figs. 2(b) and 3(a)] with $2.5 \mu\text{m}$ fiber pitch [10,11], an Omnivision OV5653 backside illuminated 5 megapixel color CMOS sensor [Fig. 3(b)] with $1.75 \mu\text{m}$ pixel pitch and image area of $4592 \mu\text{m}$ wide by $3423 \mu\text{m}$ high [12], and a fiber-coupled sensor formed by bonding the fiber bundle to the sensor using UV-cured

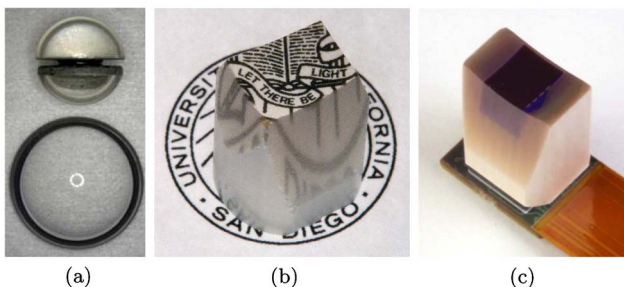


Fig. 2. (a) Monocentric lens (MC) comprised of a symmetric two-glass achromat (top) and meniscus lens (bottom). (b) Fiber bundle relays a business card logo from its flat to its curved surface. (c) Fiber bundle coupled to a sensor using optical epoxy.

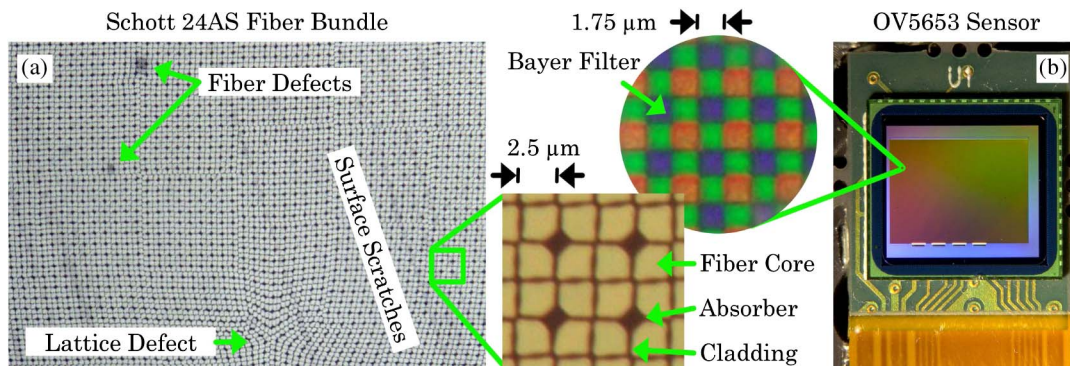


Fig. 3. (a) Fiber bundle structure and defects lead to image artifacts. Fiber absorbers between every other 2.5 μm fiber intersection prevent crosstalk. (b) OVT5653 sensor is used to sample the image exiting the fiber bundle. The two magnified inset micrographs are of the same scale.

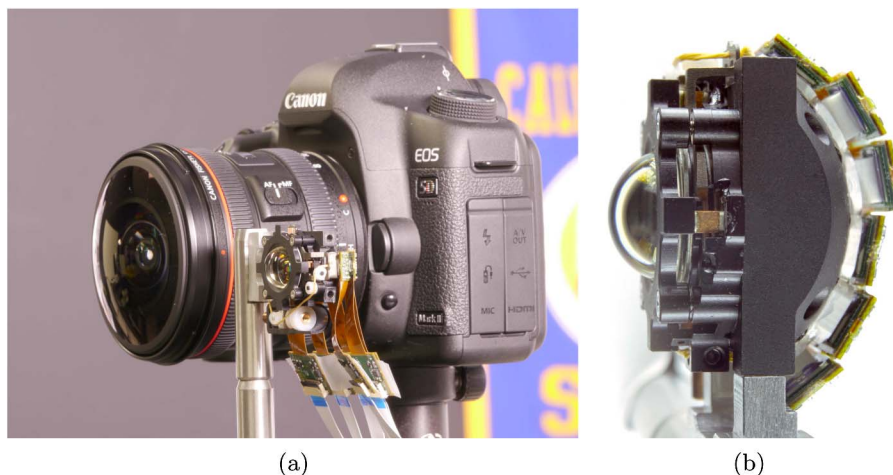


Fig. 4. (a) Side-by-side size comparison of the prototype with an $F/4$ commercial camera of similar field-of-view. (b) $F/1.35$, 30 megapixel, 126° field-of-view fiber-coupled monocentric lens imager prototype.

Norland optical adhesive NOA72 [Fig. 2(c)]. The internal structure of the fiber bundle is shown in Fig. 3(a) and leads to artifacts in the relayed imagery. A schematic and image of the cross section of the fiber-coupled sensor is shown in Fig. 5. The fiber bundle's input face has been cut and polished with a 12 mm radius of curvature to mate with the meniscus lens. A pedestal has been cut out of its exit face to mate with an image sensor whose cover glass has been removed. The schematic illustrates that the light will pass through the lens, fiber bundle, epoxy layer, lens array, and Bayer filter before it is collected by the image sensor. The epoxy layer must be kept to a minimum thickness in order to prevent the divergent light exiting the fiber bundle to defocus before it is collected by the image sensor. The fiber bundle's polished surface flatness is on the order of a wavelength, and the OV5653 surface flatness variations are approximately 1.5 μm , as measured with the Veeco NT1100 Optical Profiling System. A cross section of one of the fiber-coupled sensors confirmed a 2 μm adhesive thickness over the sensor's 1.6 μm thick lenslet and color filter. Extremely wide-angle, spatially and temporally incoherent light emission

through these surface and interface conditions do not generate high-contrast, submicron spatial patterns; therefore, negligible interference effects are detected by the sensor.

To measure the impulse response of the DUTs, we built an optical setup to simulate a moving infinitely distant point source using a white LED light behind a small (3 μm) pinhole aperture at the focal plane of a long focal length Fourier-transform lens ($f = 360$ mm, $F/ = 5.14$, and diameter $\varnothing = 76$ mm) (Fig. 6). The pinhole and LED are both mounted on a precision translation stage and shifted in small lateral steps to characterize the highly localized spatial variations in the impulse response of the DUTs. The total translation corresponded to a 25 μm displacement at the DUT and was discretized into 200 steps. For each step, an image was captured, and all images were then used to form the 3D data cubes shown in Fig. 7 and the data projections in Fig. 8. To form the data cube, the image frames in x, y are stacked up along z . The x, y coordinates of the data cube are in the pixel domain of the sensor. The z axis contains the individual photographs captured by the sensor for each step of the point source

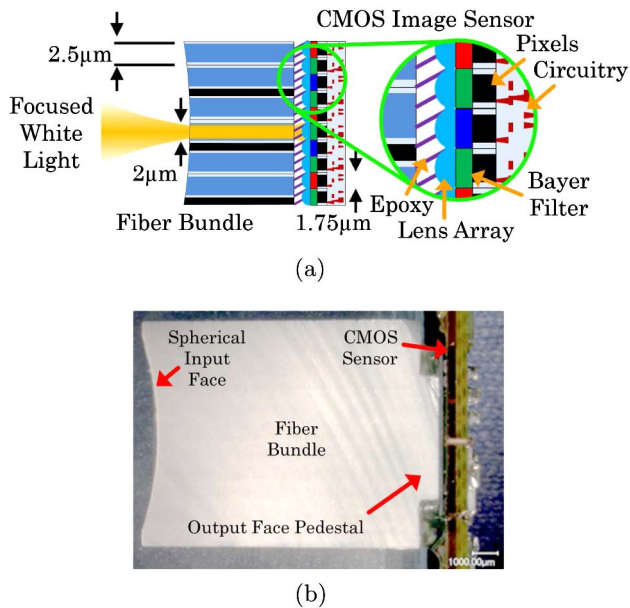


Fig. 5. (a) Schematic and (b) cross section showing the internal structure and scale of the fiber-coupled sensor. The fiber bundle relays light incident at its surface to the CMOS image sensor through an epoxy bonding layer, lens array, and Bayer filter.

translation. Projections onto each coordinate axis plane are used to help interpret the data. The projection onto the bottom plane shows the integrated response of the sensor for all frames captured during translation. Projections onto the two side planes show the behavior due to the translation, where each frame is integrated in one dimension to form these side projections. We repeated this process for each

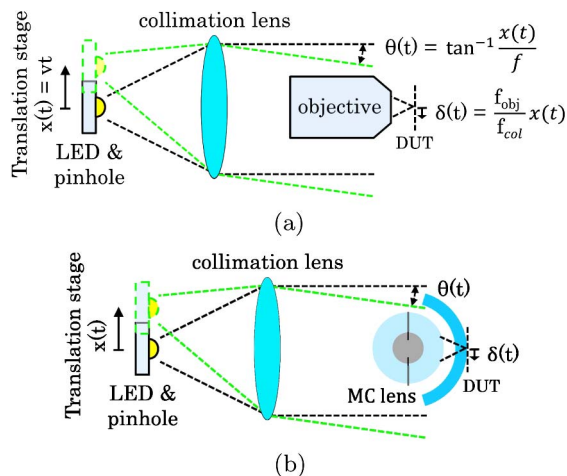


Fig. 6. Schematic of the impulse response characterization setup where an LED, pinhole, and collimation lens ($f = 360$ mm, $F/\# = 5.14$, $\varnothing = 76$ mm) form a collimated point source. Setup in (a) uses a high-resolution microscope objective ($f = 1.33$ mm, $NA = 0.9$) to characterize the monocentric lens in setup (b). Light emitted by the LED is focused onto a DUT. Translation stage is used to move the point source so that the focused spot moves $25 \mu\text{m}$ laterally across the surface of the DUT. This characterization is done to measure the local spatial variance of the impulse response for each DUT. The DUTs are a fiber bundle, sensor, and fiber-coupled sensor (see Fig. 8).

DUT using the microscope objective and monocentric lens. Figure 8 presents the data collected but only shows two of the three projections of the data cube, namely, the x - y pixel-pixel sensor domain and the x - z pixel-distance domain.

A Nikon LU Plan APO 150X microscope objective ($1.6 \mu\text{m}$ spot size) was used to illuminate each DUT to produce the data in the top row of Fig. 8, while a custom monocentric lens ($2.6 \mu\text{m}$ spot size) illuminated each DUT producing data shown on the bottom row of Fig. 8 [see schematics in Figs. 6(a) and 6(b), respectively]. The spot size was defined by the e^{-2} intensity level. For comparison, Figs. 8(a) and 8(e) show the ideal impulse response of the microscope objective and monocentric lens, respectively (measured using a 1600×1200 resolution, $4.4 \mu\text{m}$ pixel pitch Keyence VHX-1000 microscope with a $20\times$ optical magnification lens VH-Z100UW of $NA < 0.48$ and exposure time of $1/60$ th of a second). Both follow the image of the translated point source smoothly and continuously, meaning these devices are spatially invariant. The width of the line corresponds to the spot size produced by each lens, namely, 1.6 and $2.6 \mu\text{m}$. Figures 8(b) and 8(f) show the same impulse response measured using an Omnivision 5653 sensor without any optical magnification. The Bayer-filtered $1.75 \mu\text{m}$ pixels cause the spatial quantization in image sensor space. The difference in the slope in Fig. 8(f) when compared to the rest of the figure is due to the index-matching fluid-filled gap between the planar sensor and spherical image surface. Figures 8(c) and 8(g) show the same impulse response as Figs. 8(a) and 8(e) after being relayed by the fiber bundle and measured with the Keyence microscope. These images exhibit large variation in transmission depending on the location of the impulse relative to the fiber structure, but this is primarily due to the light's higher divergence angle at the fiber's exit face (when incident at the noncore regions), which cannot be captured because it is beyond the microscope's numerical aperture. Figures 8(d) and 8(h) show data collected by a image sensor coupled directly to the exit face of the fiber bundle. There is some image spread but more uniform energy transmission. A similar evolution of the impulse response of the DUTs in Figs. 8(e)–8(h) is also seen in the corresponding data in Fig. 7.

Figures 8(c), 8(d), 8(g), and 8(h) show the same measurements as in Figs. 8(a), 8(b), 8(e), and 8(f), except a fiber bundle is introduced into the system to relay the image. The fiber bundles used in our system were made by Schott using 24AS glass, with a five-sided core structure and a $2.5 \mu\text{m}$ pitch (for more information, see [10,11]). Figures 8(c) and 8(g) show that the fiber bundle impulse response is extremely spatially variant on a fine spatial scale (on the order of the pixels), allowing a large signal to pass when light is incident on one of the fiber cores. Note here that the fiber bundle does transmit light incident on noncore regions, but that the Keyence microscope's numerical aperture ($NA < 0.48$) does not collect the

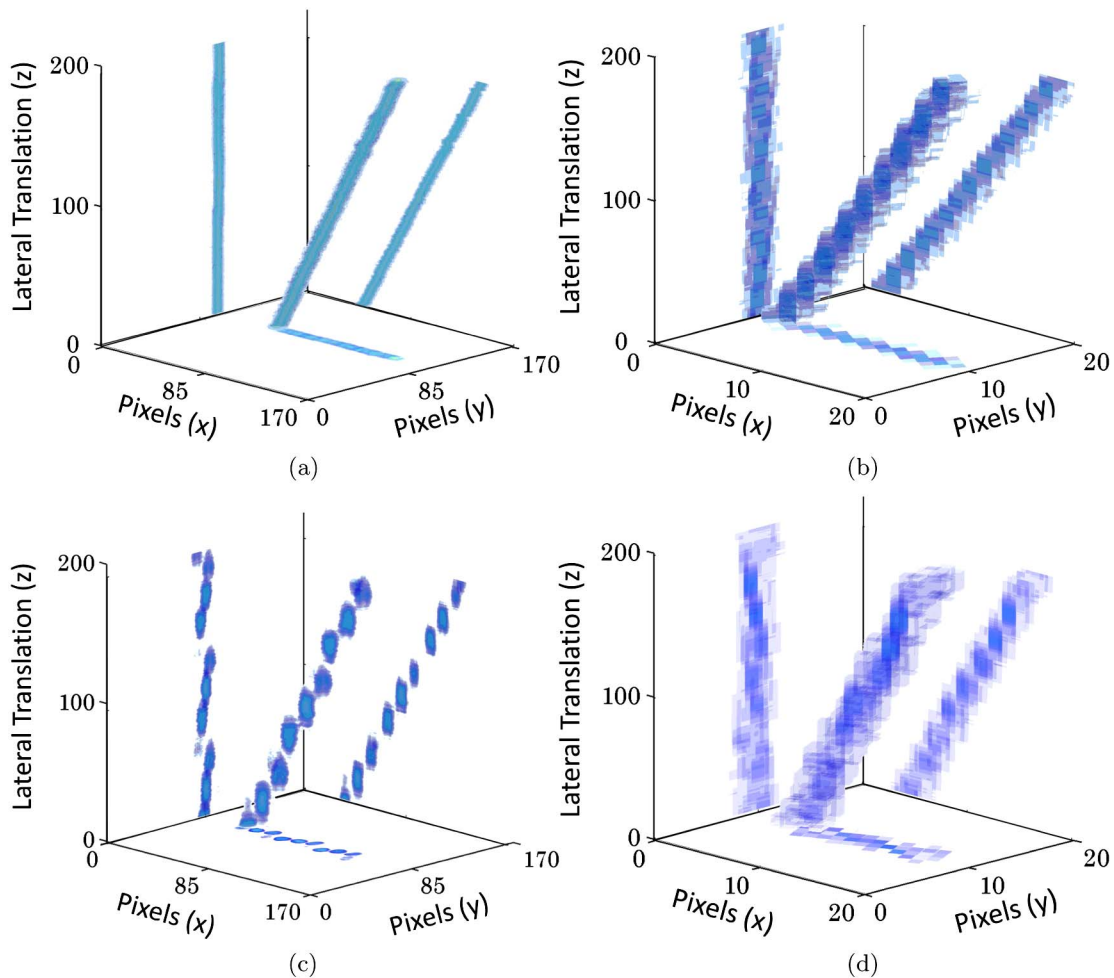


Fig. 7. Data cube representation of the impulse response of various DUTs corresponding to the bottom row of Fig. 8 collected using the setup shown in Fig. 6(b). The x - y axes correspond to the image sensor space, while the z axis is formed by stacking up 200 images taken during the 25 μm translation of a point source.

highly divergent emitted light. However, this divergent light is detected by a CMOS sensor placed in contact with the fiber bundle. Spatially variant impulse response behavior severely limits the image processing that can be used on such a system. Fortunately, Figs. 8(d) and 8(h) show that a fiber bundle that has been bonded to an image sensor exhibits considerably less spatial variance than the fiber bundle alone [see Figs. 8(c) and 8(g)]. This study shows the evolution of the impulse response behavior at the various stages within the fiber-coupled monocentric lens imager. It reveals that, although the impulse response is highly spatially variant within the system, the end-to-end system performance is in general not highly spatially variant. This enables us to use image processing techniques such as deconvolution [13,14] in order to deblur images or extended depth-of-focus in order to improve image quality [15,16].

3. Global Artifact Removal Calibration of the Fiber-Coupled Sensor and Prototype

The fiber bundle's internal structure produces an occlusion pattern that is superimposed on the images it

transfers. Strong sampling effects unique to fiber-coupled imagers are produced when the irregular fiber lattice and periodic pixel lattice are of comparable pitch, which leads to misalignment between the lattice sites, causing moiré patterns. There have been efforts to remove the occlusion effects related to fiber bundle image relay using techniques such as spatial filtering [17], Gaussian smoothing [18], or a Bayesian framework [19]. However, all of these techniques reduce image resolution. The objective here is similar to work presented in [18,19] with more general obscuration/occlusion removal techniques documented in [20–24].

Modern CMOS focal planes achieve high apparent uniformity using flat-field calibration and analog processing that substantially masks unavoidable point defects, local variations in sensitivity, and fixed pattern noise. Flat-fielding has been used to correct fiber relayed images [25] and spectra [26]. We applied a similar process to calibrate the fiber-coupled sensor by experimentally acquiring a flat-field obscuration map for a rigidly attached fiber-coupled sensor or fiber-coupled monocentric lens imager. This map

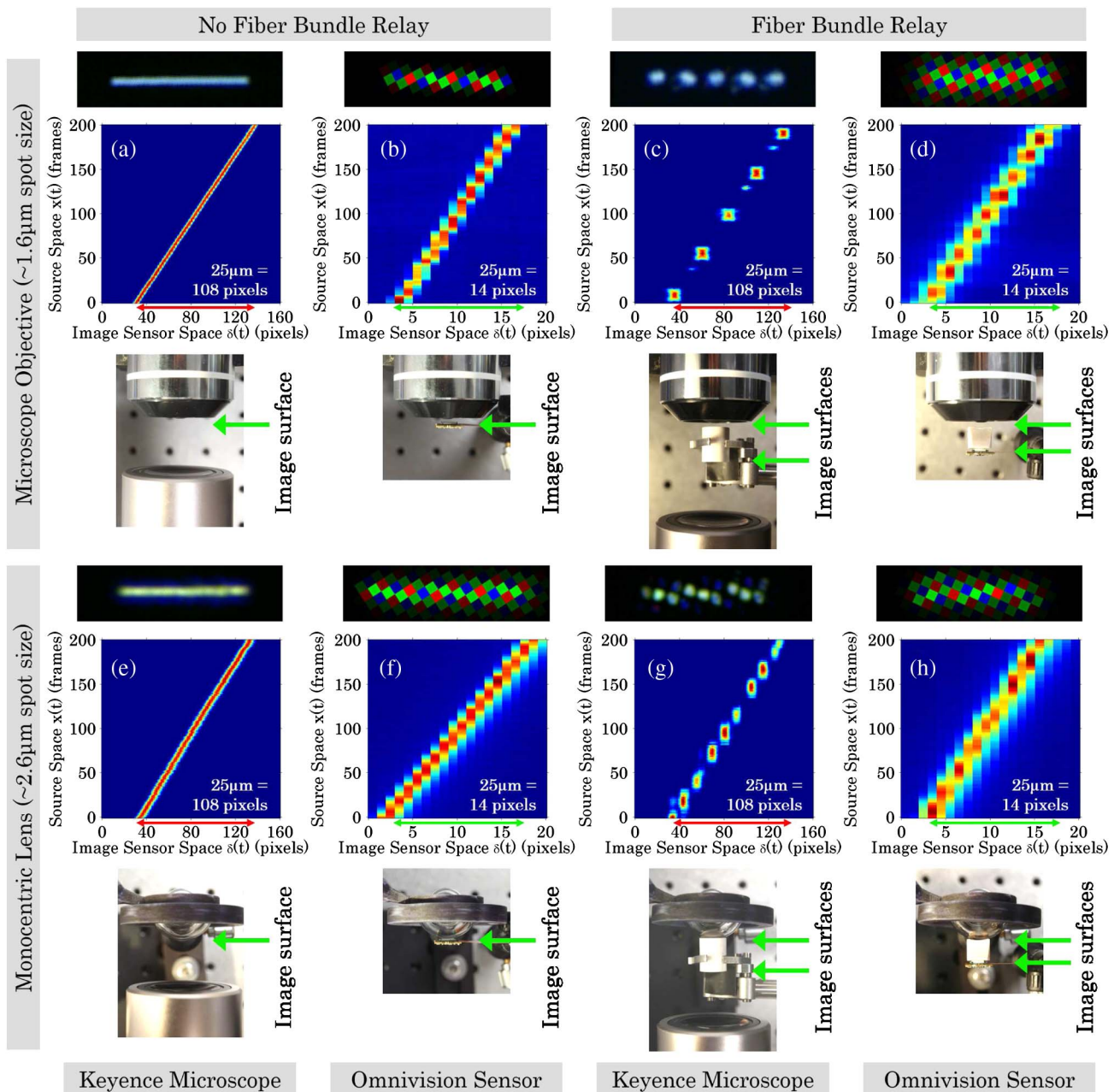


Fig. 8. Impulse characterization of system components where each subfigure contains (from top to bottom) the integration of the 200 images captured during a point source scan, a projection of the data onto translation-pixel space (see Fig. 7), and an image of the setup. These plots show the focus and linearity for each DUT. (a)–(d) and (e)–(h) were captured using the setups in Figs. 6(a) and 6(b), respectively. The difference in the slope of the data presented in 6(f) is due to the planar sensor being placed at the spherical image surface, which introduces an index-matching fluid-filled gap at the edges where light propagates before reaching the sensor. Although the intermediate response is spatially variant 6(g), invariance is recovered by the complete prototype 6(h). This extends the applicable image processing techniques that can be used.

quantifies artifacts that affect the system across the overall image space, whether introduced by the fiber structure or coupling among lens, fiber bundle, and sensor. It also allows correction of field nonuniformity due to radial vignetting due to the angle of incident light on the fiber's input face as well as lens vignetting. The flat-field obscuration map is essentially an image of an evenly illuminated white planar target object acquired by the imaging system. The

target should provide uniform illumination free of any structure and does not require the target be in focus. The dark-field image is used to account for the dark current. These artifacts due to the lens, fiber bundle, adhesive, and sensor can have higher order dependence on system temperature (due to differential thermal expansion) or sensor gain and exposure settings (due to nonlinear sensor response), leading to the use of either multiple calibration

Table 1. Statistics Taken over the Same White Part of the Images in Fig. 10 before and after Occlusion Removal Show the Process Significantly Improves Image Uniformity

| Color Channel | Uncalibrated Image [Fig. 10(b)] | | Calibrated Image [Fig. 10(c)] | |
|---------------|------------------------------------|-----------|----------------------------------|-----------|
| | Mean | Std. Dev. | Mean | Std. Dev. |
| Red | 178.35 | 20.59 | 219.27 | 9.78 |
| Green1 | 175.34 | 23.88 | 215.24 | 7.69 |
| Green2 | 174.04 | 24.52 | 215.16 | 7.71 |
| Blue | 159.86 | 17.73 | 214.48 | 6.87 |

images or a parametrized response function. This idea was presented in [27,28], which used multiple calibration images to deal with nonlinear intensity response. This is a topic of ongoing research, but preliminary results indicate the approach is robust to moderate temperature variations (20C) and a range of exposures.

The flat-field calibration images show that the finely structured global attenuation moiré pattern that overlaid the image is deterministic (Fig. 9). The most attenuated values fall to a level of about 65% of the peak intensity on-axis [Fig. 9(a)].

Figure 9(b) shows the vignetting effects that lead to the significant attenuation (see left side of the calibration image) and shifting of the histogram. Even in this case, the signal level is above 10% of the peak intensity. In both cases, the distribution that centered below the 10% value corresponds to a region of the sensor, which is not coupled to the fiber bundle (dark regions at the edge of the calibration images) and can be ignored since it does not contain image data. For these reasons, the flat-field calibration image can be used to amplify the signal of subsequent images. Figure 10 shows the calibration image (a) taken of a flat white scene, an image taken of an indoor laboratory scene (b), and the corrected image (c). The correction was made by element-wise division, which compensated for attenuation of the signal. The normalization factor for each pixel was obtained from the corresponding pixel within the calibration image. In the most attenuated regions of the image, this process was still extremely effective. Noise in the flat-field calibration image is amplified and can be significant in darker regions of the image, which require strong amplification. Although the effects are not significant in our results, they can be

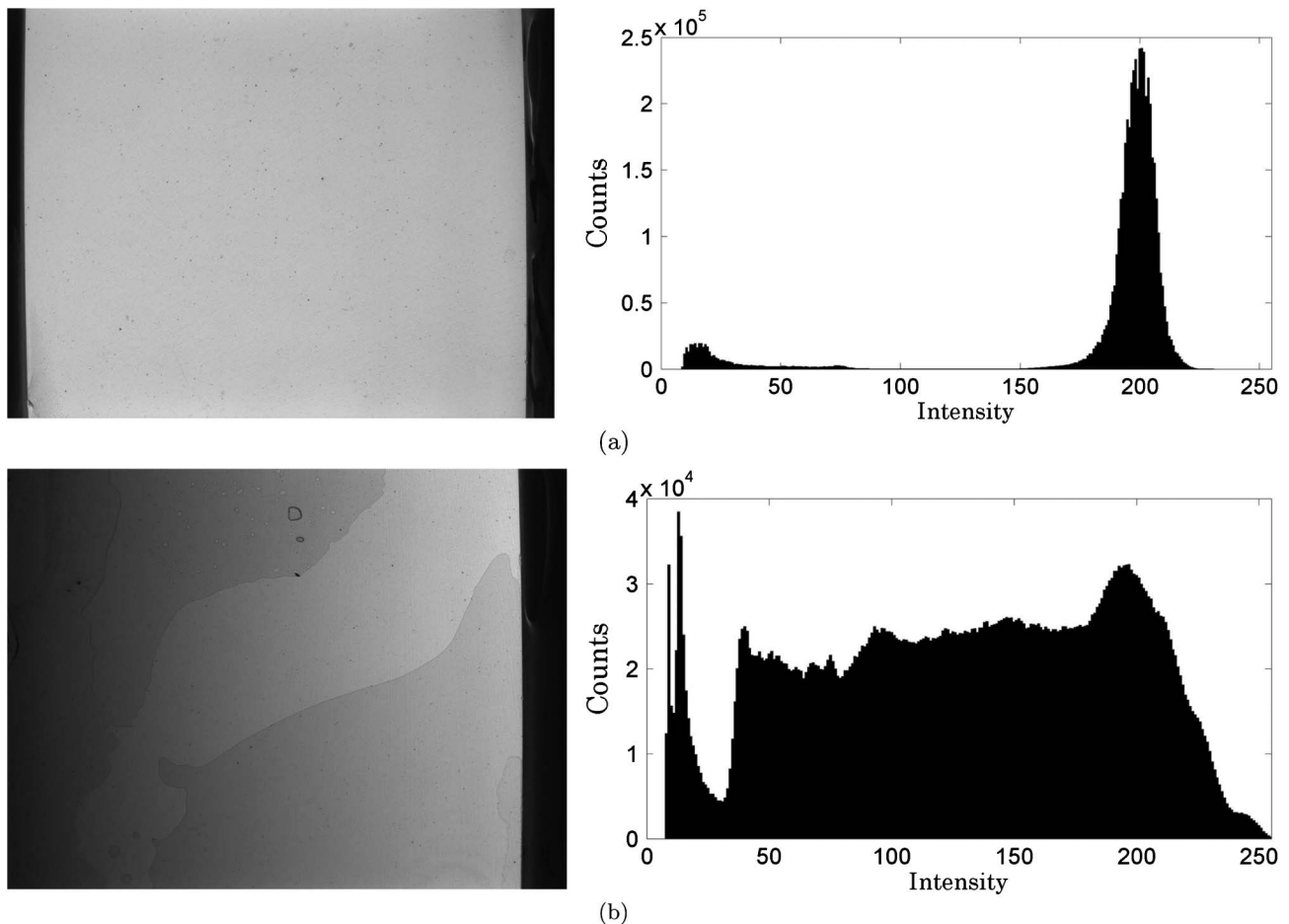


Fig. 9. Two typical flat-field calibration images (left) and their histograms (right) captured using the fiber bundle relayed imager. The lowest intensities transmitted by the bundle are above 175 (65%) (a) on-axis and 25 (10%) (b) off-axis on an 8-bit scale. Off-axis intensity transmission suffers from vignetting. The intensity values below 10% correspond to a region of the sensor where there is no fiber bundle image relay and can, therefore, be ignored. The large scale structure in (b) is due to delamination in the optical adhesive; yet, this calibration is still effective.

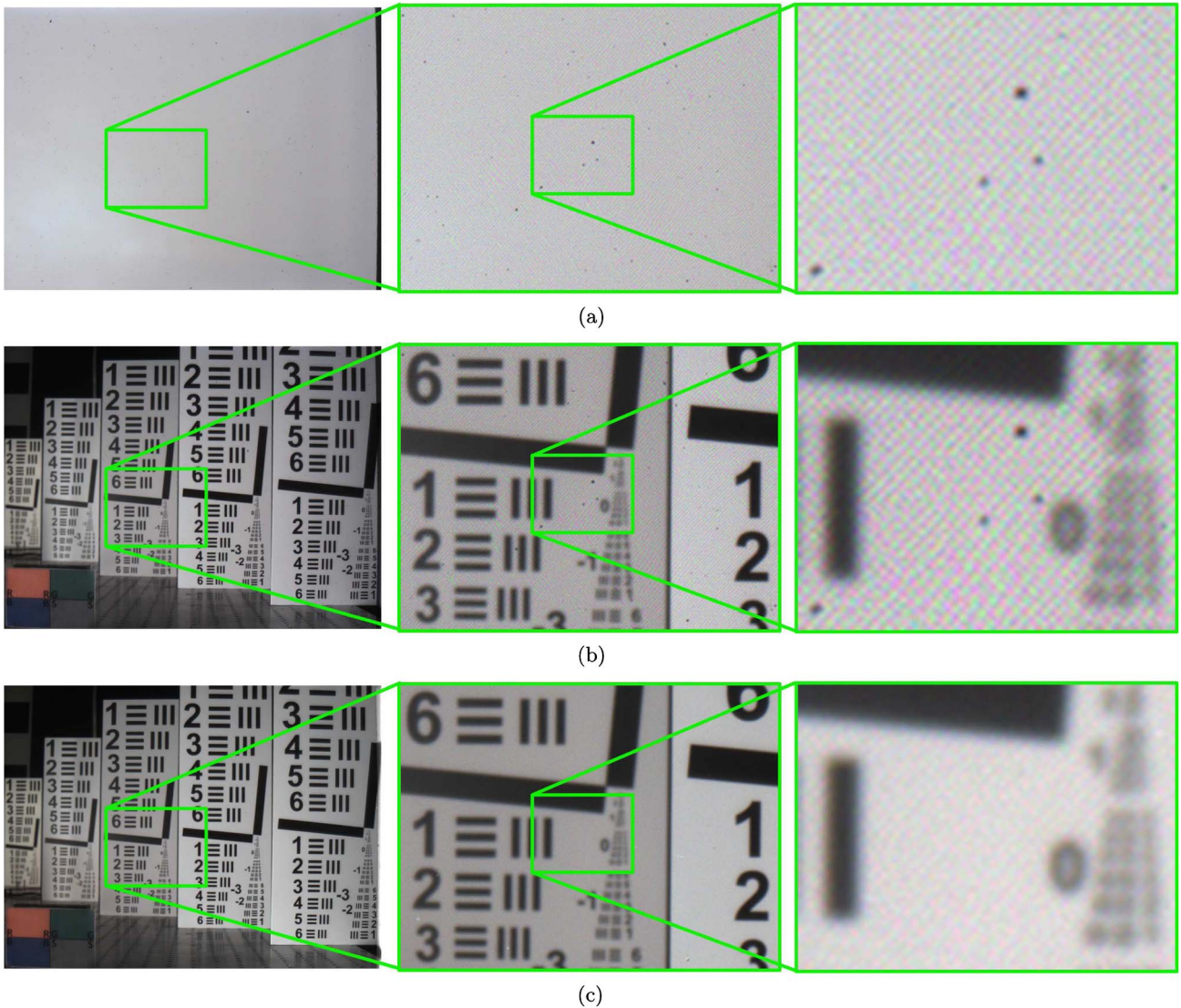


Fig. 10. Calibration image of a flat white scene (a) shows artifacts due to broken fibers, scratches, and other imperfections as well as the fiber bundle's internal structure, all of which lead to obscuration and color artifacts (b). These artifacts inherent to fiber bundle imaging are corrected using a calibration image (c). The center white region in the magnified views of (b) and (c) are used to quantify the calibration's effectiveness (see Table 1).

reduced by averaging multiple dark-field and flat-field images, respectively. Areas that may not be remedied by this process, regions of the calibration image where the signal was below a certain threshold, could have been further corrected by interpolating from nearby regions. Table 1 quantifies the improvement in uniformity over a uniform white area in Figs. 10(b) and 10(c). It was shown in [29] that the flat-fielded images still contain remnants of moiré "beat patterns," which can be used to measure fiber bundle distortion. This residual variation is evident in the calibrated image in Fig. 10(c) and its corresponding statistics in Table 1.

4. Spherical to Planar Mapping, Image Alignment, and Stitching Together Image Seams

Even with an ideal lens, there is an intrinsic distortion associated with mapping a portion of a spherical

image onto a flat image sensor, and the distortion is increasingly apparent as the field-of-view recorded with a single sensor increases. This distortion can be corrected using one of several general mathematical transformations [30]. The mapping of a direct spherical projection onto a plane is given by $s = 2r - Rr / \sqrt{R^2 - r^2}$, where the radial distance r is transformed into a scaled form s . R is the radial distance from the point where the spherical surface tangent plane is orthogonal to the sensor plane. Here Cartesian coordinates are transformed into azimuth-elevation global coordinates. Each sensor is mapped radially in this way to correct for radial pin-cushion distortion and to aid in stitching individual sensor data to form panoramas.

Assembly of the imager involves affixing the fiber-coupled sensor modules to the lens system. In addition to cutting the input and output faces of

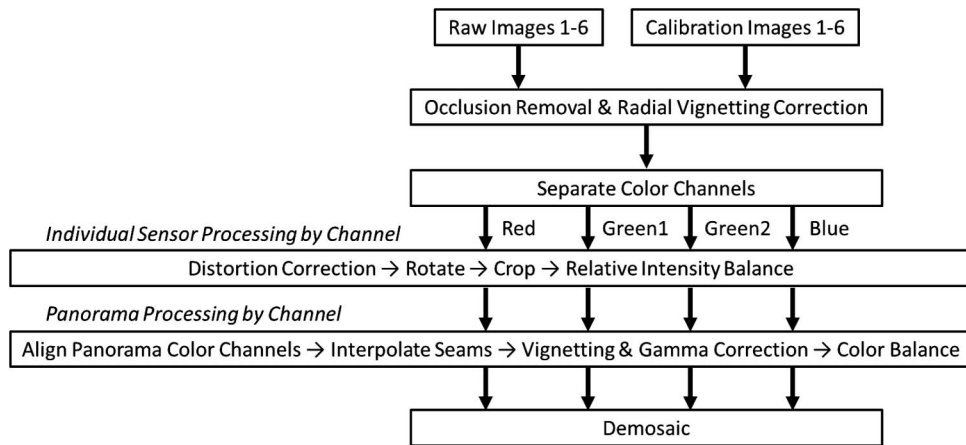


Fig. 11. Image processing data flow.

the fiber bundles, the sides are also cut such that multiple fiber-coupled sensors can fit together closely to form a contiguous sphere of the same radius as the meniscus lens so the two can interface. Physical alignment of the modules within the system is subject to error but, once assembled, is constant for the lifetime of the system. The width of the seams is limited by fiber shaping methods, which ultimately may be comparable or smaller than that of the fiber cores. But, even with near-perfect alignment, there will be some information loss at the seams (if only spreading signals between conjoined fibers), and the current prototype imager is far from this ideal. Overlapping the image boundaries would greatly facilitate stitching the image boundaries but is not possible with the current design and would require greatly increasing camera size and complexity. Here, we describe the part of the overall processing flow (Fig. 11) that follows occlusion removal and radial vignetting

correction. We separate the occlusion and radial vignetting corrected images from the various sensors into their four Bayer color channels, process them to form four panorama color channels, and then demosaic them into a color panorama. The active area of the individual sensors is not fully illuminated by the image being relayed by the fiber bundles. The images from the different sensors must be distortion corrected, rotated, cropped, and intensity balanced prior to the individual image data alignment needed to form a contiguous panorama for each color channel. One-dimensional interpolation from each boundary edge of valid data is used to restore lost data at the image seams. Vignetting effects are compensated using a modified ramp function to amplify the lower signals that appear at the extreme field angles. Gamma correction is then performed on the four color channel panoramas. After the four color channels are processed as described to form panorama

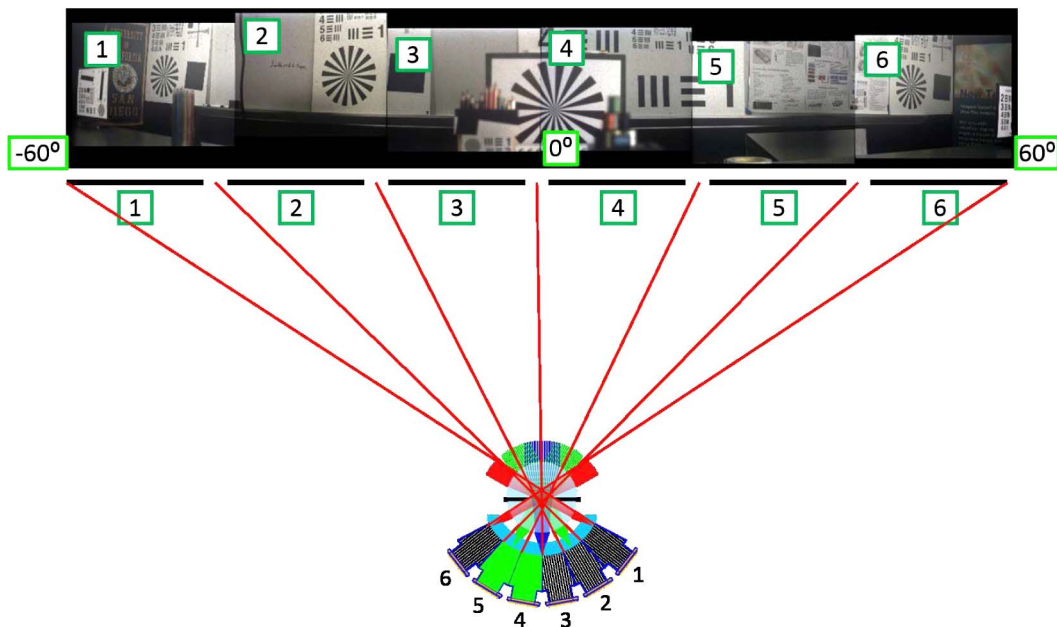
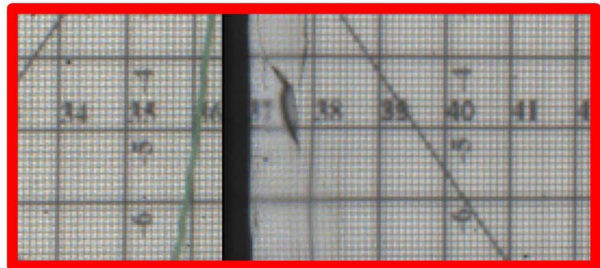
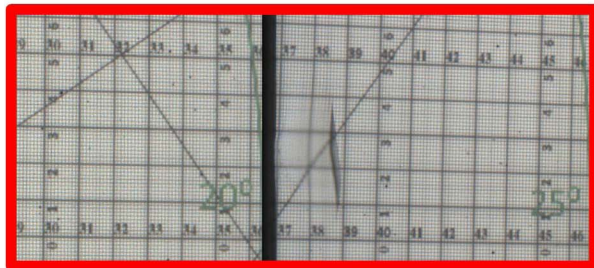
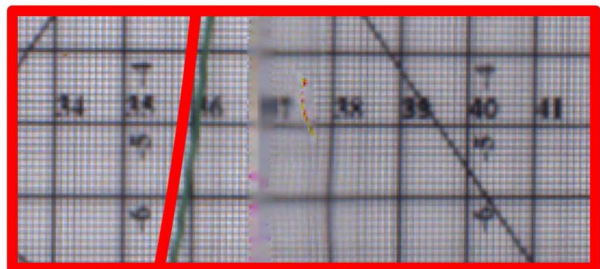
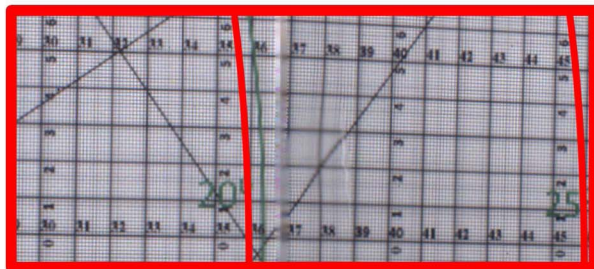
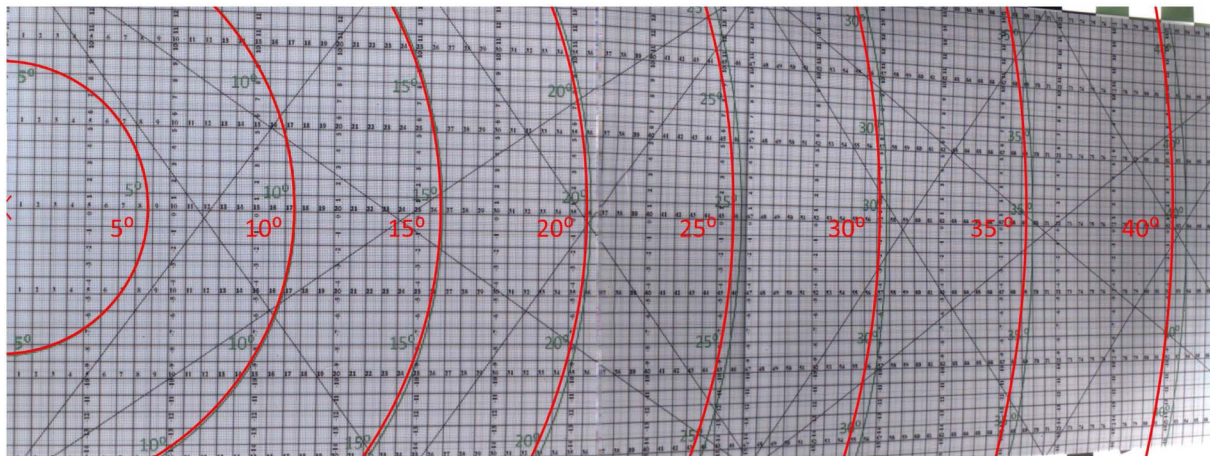


Fig. 12. Schematic showing the fiber-coupled sensors in the prototype and their respective field-of-view. The six sensors gather image data across a 126° field-of-view.



(a)



(b)

Fig. 13. Distortion correction and image stitching. (a) Unprocessed sensor data from two individual sensors [Sensors 4 and 5 in Figs. 1(b) and 12] show barrel distortion and information loss at the sensor adjacent boundary. (b) Distortion is corrected, and the seam is interpolated to stitch the images together. The ground-truth mapping angle markings are shown in red to indicate residual error in distortion correction.



Fig. 14. Image taken using a conventional wide field-of-view camera (Canon 5D mark II with EF 8–15 mm $F/4$ fisheye lens) with similar characteristics as the fiber-coupled monocentric lens imager. Magnified regions show the image resolution.

color channels, they are interpolated to form a single white balanced color panoramic image.

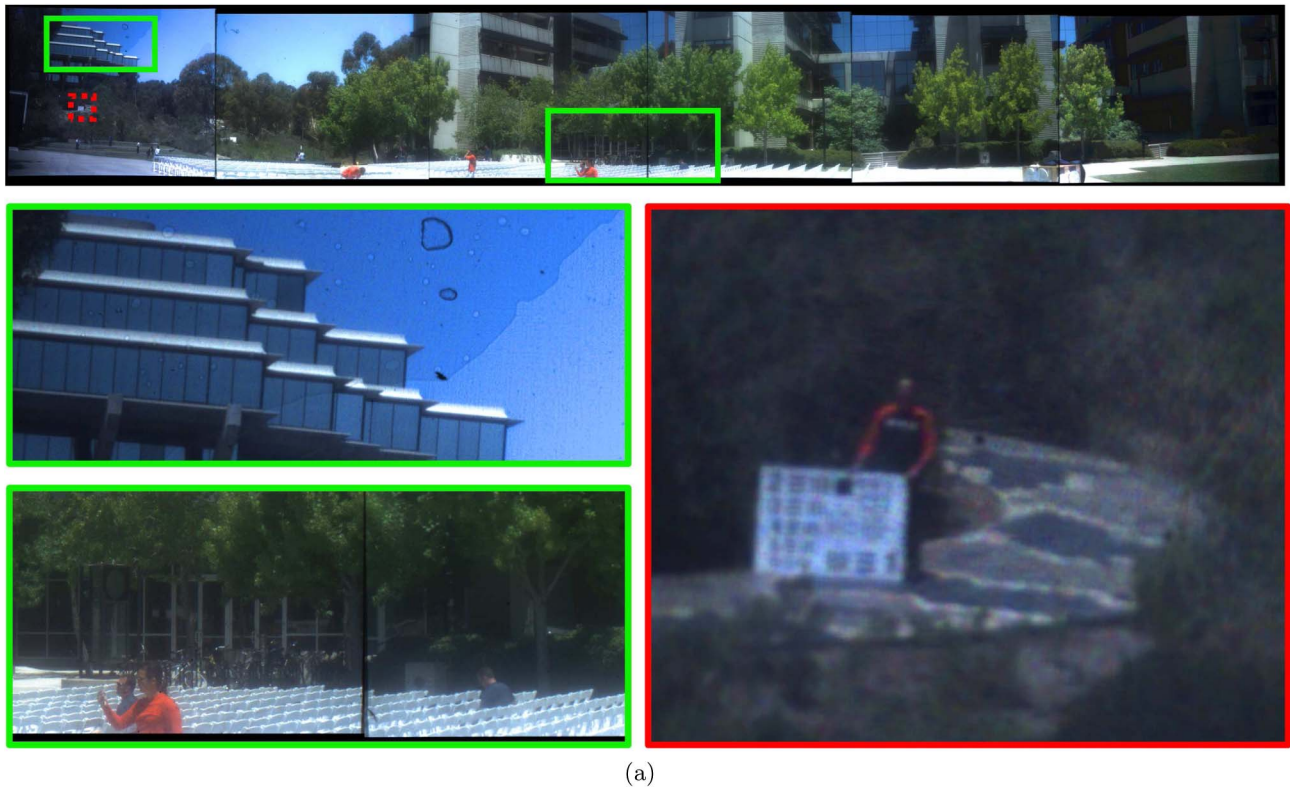
The highly localized structural and color artifacts due to the fiber bundle limit the effectiveness of demosaic interpolation techniques that rely on texture, edges, or gradient image content. After evaluating several interpolation techniques, we found that bilinear interpolation produced the best resulting images. A global saturation adjustment was used to compensate for the sensor's color response. The steps in the methodology mentioned here were selected out of a large class of techniques and can be modified or replaced. For example, the stitching process documented in [31] is effective at balancing the content across seams that exhibit discontinuous content due to flawed image performance, producing a much less noticeable image boundary.

5. Experimental Setup

Experimental data were collected in the lab with the monocentric lens using two adjacent fiber-coupled sensors corresponding to Sensors 4 and 5 in Figs. 1(b) or 12. One sensor imaged the scene from 0° on axis to 20° , and the other sensor imaged from 20° to 40° . This image boundary was chosen because it well represented an arbitrary image seam since it was not along the optical axis. The planar scene was positioned at an orthogonal distance of 1 m from the camera along the optical axis. The scene was a flat printed grid (designed to be 1 m from the camera) with centimeter markings and concentric circles denoting the angle deviation from the optical axis.

Laboratory data (Fig. 13) enabled us to quantify distortion correction and the amount of information loss at the image boundary between closely tiled adjacent sensors, which corresponded to 2 mm in object space at a distance of 1 m or 0.2° . From this characterization, we can accurately stitch the scene together. The calibration described here needs to be calculated only once since the monocentric lens imager parts are held fixed by adhesive, with the exception of color balance which is affected by the ambient illumination spectrum. This sufficiently characterizes the imager so that significantly improved panoramas can be processed from the individual raw image sensor data. The complete systematic methodology we used to process the fiber-coupled monocentric lens image data is documented in Fig. 11. Partially and completely processed images resulting from this process are shown in Fig. 13. In what follows, we demonstrate that this process enables the fiber-coupled monocentric lens imager to produce artifact-limited panoramas that suffer from less aberrations and distortions than traditional wide FOV lenses.

We compared the performance of the prototype against a commercially available camera (Canon 5D mark II with EF 8–15 mm $F/4$ fisheye lens) by taking images of the same outdoor scene under identical conditions. The outdoor scene was imaged using all six fiber-coupled sensors within the $F/1.35$ fiber-coupled monocentric lens imager to form a $126^\circ \times 16^\circ$ panorama (see Fig. 12). The prototype has a $126^\circ \times 16^\circ$ field-of-view and resolution of 30 megapixels that



(a)



(b)

Fig. 15. (a) Unprocessed and (b) processed fiber relayed prototype image data of a panorama showing significant image improvement attributed to the image processing methodology. Artifacts due to bubbles in the optical adhesive, broken fibers, and fiber bundle scratches are effectively removed by flat-field calibration. The flat-field calibration images for Sensors 1 and 4 (from right) are shown in Fig. 9. Distortions are corrected, the images aligned, and missing data is interpolated in order to form the processed panorama. Magnified regions show that the prototypes resolution is superior to the benchmark camera images shown in Fig. 14.

can be increased by incorporating more fiber-coupled sensors. The ground-truth comparison image is

shown in Fig. 14. This comparison camera was chosen, since it was designed to meet similar

performance specifications without being limited to a small form factor. Figure 15 exemplifies the improvement our methodology provides to fiber relayed imagery. Of particular interest is the removal of artifacts due to bubbles (in the optical adhesive used to mate the lens with the fiber), broken fibers, and scratches. This first prototype suffered from more of these effects than subsequent prototypes; however, we chose to include this imagery, since it best illustrates the efficacy of the techniques described. Additionally, the significant vignetting effects at the edges of the wide angle panorama are corrected for using an amplification map. Distortion correction and interpolation of missing data at the boundaries allows the formation of panoramic imagery. The composite image demonstrated in Fig. 15(b) shows that, by using fiber bundle image relay along with the techniques described here, we are now able to use lenses (that form nonplanar image surfaces and are otherwise incompatible with current technology) in order to form high-resolution images with less distortion than that of the commercial alternative. Magnified views (enclosed in red) inset in Figs. 14 and 15 show a portion of the scene that is about 50° left of center and 150 m downrange for both comparison cameras. This comparison shows the prototype exhibits less distortion, less chromatic aberration, and a large boost in resolution.

6. Discussion and Conclusion

This paper summarizes the characterization and image processing for imaging systems that uses fiber bundle image relay, including a component-by-component transfer function characterization of the fiber-coupled imager. We found that the high spatial variance of some of the individual components is reduced when used in conjunction with other components, allowing for more flexibility when implementing image processing techniques. We experimentally demonstrated how flat-field correction proves beneficial for fiber-coupled imaging systems by correcting for the response of the lens, fiber bundle, and sensor, all of which produce fixed pattern artifacts. We showed how to stitch together panoramas taking into account artifacts, image transfer uniformity, mapping, and the registration of individual sensor data prior to interpolation of image information not captured between adjacent sensors. Using this methodology, we formed a 30 megapixel 126° field-of-view fiber-coupled panoramic image, which compares favorably in image resolution and distortion to the benchmark commercial camera whose volume (for lens and sensor only) is more than 10 times the fiber-coupled prototype.

Support was provided by the DARPA SCENICC program contract W911NF-11-C-0210. The authors thank Glenn Schuster, William M. Mellette, Salman Karbasi, and Nojan Motamedi for technical discussion and laboratory support.

References

1. R. Kingslake, *A History of the Photographic Lens* (Academic, 1989), pp. 49–67.
2. I. Stamenov, I. P. Agurok, and J. E. Ford, “Optimization of two-glass monocentric lenses for compact panoramic imagers: general aberration analysis and specific designs,” *Appl. Opt.* **51**, 7648–7661 (2012).
3. S.-B. Rim, P. B. Catrysse, R. Dinyari, K. Huang, and P. Peumans, “The optical advantages of curved focal plane arrays,” *Opt. Express* **16**, 4965–4971 (2008).
4. N. S. Kapany, J. A. Eyer, and R. E. Keim, “Fiber optics. Part II. Image transfer on static and dynamic scanning with fiber bundles,” *J. Opt. Soc. Am.* **47**, 423–425 (1957).
5. R. Drougard, “Optical transfer properties of fiber bundles,” *J. Opt. Soc. Am.* **54**, 907–914 (1964).
6. T. S. Axelrod, N. J. Colella, and A. G. Ledebuhr, “The wide-field-of-view camera,” in *Energy and Technology Review* (Lawrence Livermore National Laboratory, 1988), pp. 1–12.
7. J. Ford, I. Stamenov, S. J. Olivas, G. Schuster, N. Motamedi, I. P. Agurok, R. Stack, A. Johnson, and R. Morrison, “Fiber-coupled monocentric lens imaging,” in *Imaging and Applied Optics Technical Papers*, OSA Technical Digest (Optical Society of America, 2013), paper CW4C.2.
8. S. J. Olivas, N. Nikzad, I. Stamenov, A. Arianpour, G. Schuster, N. Motamedi, W. M. Mellette, R. A. Stack, A. R. Johnson, R. Morrison, I. Agurok, and J. E. Ford, “Fiber bundle image relay for monocentric lenses,” in *Computational Optical Sensing and Imaging*, OSA Technical Digest (Optical Society of America, 2014), paper CTh1C.5.
9. I. Stamenov, A. Arianpour, S. J. Olivas, I. P. Agurok, A. Johnson, R. Stack, R. Morrison, and J. E. Ford, “Panoramic monocentric imaging using fiber-coupled focal planes,” *Opt. Express* **22**, 31708–31721 (2014).
10. Schott “Fiber optic faceplates,” http://www.us.schott.com/lightingimaging/english/download/schott-faceplate_us_july_2013.pdf.
11. J. J. Hancock, *The Design, Fabrication, and Calibration of a Fiber Filter Spectrometer* (The University of Arizona, 1957).
12. Omnivision “OV5653 Color CMOS QXSGA image sensor with OmniBSI technology,” OV5653-A66A datasheet, October 2011, <http://www.ovt.com/products/sensor.php?id=68>.
13. S. J. Olivas, M. Šorel, and J. E. Ford, “Platform motion blur image restoration system,” *Appl. Opt.* **51**, 8246–8256 (2012).
14. S. J. Olivas, M. Šorel, N. Nikzad, and J. Ford, “Platform motion blur image restoration system,” in *Imaging and Applied Optics Technical Papers*, OSA Technical Digest (Optical Society of America, 2012) paper CTu2B.3.
15. H. Nagahara, S. Kuthirummal, C. Zhou, and S. K. Nayar, “Flexible depth of field photography,” in *European Conference on Computer Vision (ECCV)* (Springer, 2008).
16. S. J. Olivas, M. Šorel, A. Arianpour, I. Stamenov, N. Nikzad, G. M. Schuster, N. Motamedi, W. M. Mellette, R. A. Stack, A. Johnson, R. Morrison, I. P. Agurok, and J. E. Ford, “Digital image processing for wide-angle highly spatially-variant imagers,” *Proc. SPIE* **9193**, 91930B (2014).
17. M. M. Dickens, M. P. Houlne, S. Mitra, and D. J. Bornhop, “Method for depixelating micro-endoscopic images,” *Opt. Eng.* **38**, 1836–1842 (1999).
18. J.-H. Han, J. Lee, and J. U. Kang, “Pixelation effect removal from fiber bundle probe based optical coherence tomography imaging,” *Opt. Express* **18**, 7427–7439 (2010).
19. J.-H. Han and S. M. Yoon, “Depixelation of coherent fiber bundle endoscopy based on learning patterns of image prior,” *Opt. Lett.* **36**, 3212–3214 (2011).
20. C. Herley, “Automatic occlusion removal from minimum number of images,” in *IEEE International Conference on Image Processing 2* (IEEE, 2005), pp. II-1046–1049.
21. J. Gu, R. Ramamoorthi, P. Belhumeur, and S. Nayar, “Removing image artifacts due to dirty camera lenses and thin occluders,” *ACM Trans. Graph.* **28**, 144 (2009).
22. D. Devasruthi, H. P. Menon, and K. A. Narayanankutty, “FE-BEMD and exemplar based hybrid image inpainting

- for occlusion removal,” *Int. J. Comput. Geom. Appl.* **28**, 38–44 (2011).
23. S. McCloskey, M. Langer, and K. Siddiqi, “Removal of partial occlusion from single images,” *IEEE Trans. Pattern Anal. Mach. Intell.* **33**, 647–654 (2011).
 24. B. Antony M. and K. A. Narayanankutty, “Removing occlusion in images using sparse processing and texture synthesis,” *Intern. J. Comp. Sci. Eng. Appl.* **2**, 117–124 (2012).
 25. G. M. Lawrence, “Hex-square moire patterns in imagers using microchannel plates,” *Appl. Opt.* **28**, 4337–4343 (1989).
 26. W. Curdt, D. Germerott, K. Wilhelm, U. Schühle, L. Teriaca, D. Innes, K. Bocchialini, and P. Lemaire, “The SUMER data in the SOHO archive,” *Solar Phys.* **289**, 2345–2376 (2014).
 27. J. A. Seibert, J. M. Boone, and K. K. Lindfors, “Flat-field correction technique for digital detectors,” *Proc. SPIE* **3336**, 348–354 (1998).
 28. A. L. C. Kwan, J. A. Seibert, and J. M. Boone, “An improved method for flat-field correction of flat panel x-ray detector,” *Med. Phys.* **33**, 391–393 (2006).
 29. A. S. Tremsin, O. H. W. Siegmund, M. A. Gummin, P. N. Jelinsky, and J. M. Stock, “Electronic and optical moiré interference with microchannel plates: artifacts and benefits,” *Appl. Opt.* **38**, 2240–2248 (1999).
 30. R. Szeliski, “Image alignment and stitching: a tutorial,” *Found. Trends. Comput. Graph. Vis.* **2**, 1572–2740 (2006).
 31. G. Ward, “Hiding seams in high dynamic range panoramas,” in *Proceedings of the 3rd Symposium on Applied Perception in Graphics and Visualization* (ACM, 2006), p. 150.